A R C H I V E O F M E C H A N I C A L E N G I N E E R I N G

VOL. LXIII 2016 Number 2

10.1515/meceng-2016-0016

Key words: geometrically exact shell; flexible multibody dynamics; tire modelling; unilateral contact

MICHAEL ROLLER [*], *PETER BETSCH* [**], *AXEL GALLREIN*[*], *JOACHIM LINN*[*]

AN ENHANCED TIRE MODEL FOR DYNAMIC SIMULATION BASED ON GEOMETRICALLY EXACT SHELLS

In the present work, a tire model is derived based on geometrically exact shells. The discretization is done with the help of isoparametric quadrilateral finite elements. The interpolation is performed with bilinear Lagrangian polynomials for the mid-surface as well as for the director field. As time stepping method for the resulting differential algebraic equation a backward differentiation formula is chosen. A multilayer material model for geometrically exact shells is introduced, to describe the anisotropic behavior of the tire material. To handle the interaction with a rigid road surface, a unilateral frictional contact formulation is introduced. Therein a special surface to surface contact element is developed, which rebuilds the shape of the tire.

1. Introduction

Acting as an interface between the car and the road, the tire model plays an important role in dynamic vehicle simulations. In commercial and scientific applications there exist several different modeling approaches for tires. When the tire model has to be embedded into a multi body system (MBS), lumped parameter models of varying complexity consisting of springs and dampers [10] are used, as well as simple data curve fits [13]. Very detailed but computationally demanding three dimensional finite element (FE) models are used for crash and misuse simulations [14]. A coupling of such 3D-FE tire models to MBS simulations is mostly not feasible due to the large number of degrees of freedom. Our purpose is to develop a continuum

[*] *Fraunhofer Institute for Industrial Mathematics, Fraunhofer Platz 1, 67663 Kaiserslautern, Germany; E-mails: Michael.Roller@itwm.fraunhofer.de; Axel.Gallrein@itwm.fraunhofer.de; Joachim.Linn@itwm.fraunhofer.de*

[**] *Institute of Mechanics, Karlsruhe Institute of Technology (KIT), Otto-Ammann-Platz 9, 76131 Karlsruhe, Germany; E-mail: Peter.Betsch@kit.edu*

- 10.1515/meceng-2016-0016
Downloaded from De Gruyter Online at 09/23/2016 07:41:16AM
via free access

mechanical based structural model, which requires only modest amounts of computational resources so that a coupling with a MBS simulation is viable.

In [15], a tire model based on the geometrically exact shell theory of [17] was introduced, where finite elements (FE) are used for the spatial discretization [1]. The backward differentiation formula (BDF) was chosen as time stepping method for the arising differential algebraic equation (DAE) [3]. The developed tire model is able to handle pressure loads as well as frictionless contact with a rigid road surface. Also a special kind of orthotropic material is available, where one principal direction is parallel to the normal of the midsurface. The tire model is able to interact with a MBS simulation via co-simulation, with the rim forces and displacements as interface. In this work we enhance this discrete shell based tire model from [15] by adding a multi layered material model and frictional contact.

This work is structured as follows. First the equations of motion of the discrete shell are briefly derived in Section 2. After that, in Section 3 a multi layered material model is integrated in the shell model. In Section 4 the frictional contact formulation is presented, as well as a special discretization of the contact surface. Typical tire test rig experiments are realized with the developed tire model in Section 5 and compared to reference solutions. At last we give a conclusion of our work in Section 6.

2. Equations of motion

In this section we want to indicate how the equations of motion of the discrete shell are derived. This will be done in a concise way, for more details we refer to [15]. To describe the motion of the shell in space we follow the approach from [17]. Therein the configuration of the shell is given by two functions

$$\varphi : \omega \to \mathbb{R}^3 , \qquad \mathbf{d} : \omega \to \mathsf{S}^2 . \tag{1}$$

Both are defined on a two dimensional parameter domain $\omega \subset \mathbb{R}^2$. The set $\mathsf{S}^2 := \{\mathbf{d} \in \mathbb{R}^3 | \|\mathbf{d}\| = 1\}$ represents the two dimensional unit sphere embedded in a three dimensional space. The function φ represents the midsuface of the shell and $\mathbf{d}$ a unit vector field pointing into the direction of the material fibers. Let h be the thickness of the shell, then its three dimensional configuration is given by

$$\phi(\chi, \zeta) = \varphi(\chi) + \zeta \mathbf{d}(\chi) , \qquad \phi : \Omega \to \mathcal{B} \subset \mathbb{R}^3 , \tag{2}$$

with the domain $\Omega := \omega \times \left[-\frac{h}{2}, \frac{h}{2}\right]$. The partial derivatives of the parameterization (2) define the covariant basis of the shell continuum $\boldsymbol{g}_\alpha := \phi_{,\alpha}$ and

- 10.1515/meceng-2016-0016
Downloaded from De Gruyter Online at 09/23/2016 07:41:16AM
via free access

$\boldsymbol{g}_3 := \phi_{,3}$. In this work greek indexes represent the numbers $\{1, 2\}$, while small latin letters stand for the set $\{1, 2, 3\}$. For partial derivatives the shortened notation $\phi_{,\alpha} := \frac{\partial \phi}{\partial \chi_\alpha}$ is used. The tangential vectors of the midsurface are defined as $\boldsymbol{a}_\alpha := \varphi_{,\alpha}$. The contravariant bases of the shell is defined by the system of equations $\boldsymbol{g}_i \cdot \boldsymbol{g}^j = \delta^i_j$. The metrics of the continuum are given by $g_{ij} := \boldsymbol{g}_i \cdot \boldsymbol{g}_j$ and $g^{ij} := \boldsymbol{g}_i \cdot \boldsymbol{g}_j$. The corresponding metric of the midsurface is given by $a_{\alpha\beta} = \boldsymbol{a}_\alpha \cdot \boldsymbol{a}_\beta$. As additional invariants of the shell continuum a pseudo curvature $\kappa_{\alpha\beta} := \boldsymbol{a}_\alpha \cdot \mathbf{d}_{,\beta} + \boldsymbol{a}_\beta \cdot \mathbf{d}_{,\alpha}$ and a shear field $\gamma_\alpha := \boldsymbol{a}_\alpha \cdot \mathbf{d}$ are introduced. To measure the deformation of the shell continuum, a stress free reference configuration is defined by

$$\phi_0(\boldsymbol{\chi}, \zeta) := \varphi_0(\boldsymbol{\chi}) + \zeta \mathbf{d}_0(\boldsymbol{\chi}) \,, \qquad \phi_0 : \Omega \to \mathcal{B}_0 \subset \mathbb{R}^3 \,, \tag{3}$$

where again φ_0 represents the midsurface of the shell volume and $\mathbf{d}_0$ is a unit vector field, see (1). To distinguish the reference configuration from the deformed configuration, we use capital letters for the quantities of the reference configuration. In the reference configuration it is additionally assumed that the director is perpendicular to the tangential vectors of the midsurface $\mathbf{d}_0 \cdot \boldsymbol{A}_\alpha = 0$. The deformation gradient of the mapping between the configurations $\Phi := \phi \circ (\phi_0)^{-1}$ is given by $\mathsf{F} := \nabla\Phi = \boldsymbol{g}_i \otimes \boldsymbol{G}^i$. As objective strain measure [2] we choose the Green-Lagrange tensor $\mathsf{E} = \mathsf{F}^T\mathsf{F} - \mathsf{Id}$, which may be represented as $\mathsf{E} = E_{ij}(\boldsymbol{G}^i \otimes \boldsymbol{G}^j)$. The components of this strain measure $E_{ij} := \frac{1}{2}(g_{ij} - G_{ij})$ can be decomposed in differences of the single quantities of the two configurations

$$E_{\alpha\beta} = \frac{1}{2}(a_{\alpha\beta} - A_{\alpha\beta}) + \zeta\frac{1}{2}(\kappa_{\alpha\beta} - \mathcal{K}_{\alpha\beta}), \quad E_{\alpha 3} = \frac{1}{2}(\gamma_\alpha - \Gamma_\alpha), \quad E_{33} = 0. \tag{4}$$

Because of the unit length of the director there is no strain in the E_{33} component, which is called plain strain in literature [4]. As usual all terms witch are higher order one in ζ are ignored.

The work conjugated stress measure [2] of the Green-Lagrange strain tensor is the second Piola-Kirchhoff tensor $\mathsf{S} = S^{ij}(\boldsymbol{G}_i \otimes \boldsymbol{G}_j)$. Both tensors are related through a material law. Because we only assume small local strains[1], we restrict ourselves to a linear dependency between stress and strain. Therefore, it exists a fourth order tensor $\mathbb{C} := C^{ijkl}(\boldsymbol{G}_i \otimes \boldsymbol{G}_j \otimes \boldsymbol{G}_k \otimes \boldsymbol{G}_k)$, which describes this relation $S^{ij} = C^{ijkl}E_{kl}$.

The components of the material tensor C^{ijkl} fullfill the usual symmetries [2]. To transfer this three dimensional material law to the shell, we addi-

[1] Because we choose the Green-Lagrange tensor as objective strain measure, rigid body motions of the whole shell do not contribute to the strain measure. Hence large rotations are still possible, which are necessary if we think about tire dynamics.

- 10.1515/meceng-2016-0016
Downloaded from De Gruyter Online at 09/23/2016 07:41:16AM
via free access

tionally assume that the following components of the material tensors vanish $C^{\alpha\beta\iota 3} = C^{\alpha 333} = 0$. So for the components of the strain tensor we get

$$S^{\alpha\beta} = C^{\alpha\beta\iota\pi}E_{\iota\pi} + C^{\alpha\beta 33}E_{33}, \quad S^{\alpha 3} = 2C^{\alpha 3\beta 3}E_{\beta 3}, \quad S^{33} = C^{33\alpha\beta}E_{\alpha\beta} + C^{3333}E_{33}. \tag{5}$$

By assuming plain stress ($S^{33} = 0$) we can rearrange (5) to

$$S^{\alpha\beta} = H^{\alpha\beta\iota\pi}E_{\iota\pi}\,, \qquad S^{\alpha 3} = \frac{1}{2}H^{\alpha 3\beta 3}E_{\beta 3}. \tag{6}$$

Here H^{ijkl} are the components of a shell material tensors $\mathbb{H} = H^{ijkl}(\boldsymbol{G}_i \otimes \boldsymbol{G}_j \otimes \boldsymbol{G}_k \otimes \boldsymbol{G}_k)$, which are given by

$$H^{\alpha\beta\iota\pi} = \frac{C^{\alpha\beta 33}C^{33\iota\pi}}{C^{3333}}\,, \qquad H^{\alpha 3\beta 3} = 4C^{\alpha 3\beta 3}\,, \qquad H^{3333} = 0. \tag{7}$$

2.1. Weak formulation and discretization

To solve the differential equation prescribing the motion of the shell continuum, we use the variational principle for the three dimensional problem [19] and eliminate the dependency of ζ by integration. The starting point of the problem is to find the function Φ such that for all variations $\delta\Phi$ the following holds

$$-\int_{\mathcal{B}_0} \mathsf{FS} : \delta\mathsf{F}\ \mathrm{d}\mathbf{X} + \int_{\mathcal{B}_0} \mathbf{F}_0 \cdot \delta\Phi\ \mathrm{d}\mathbf{X} = \int_{\mathcal{B}_0} \frac{\mathrm{d}^2}{\mathrm{d}t^2}\Phi \cdot \delta\Phi\ \mathrm{d}\mathbf{X}\,. \tag{8}$$

The vector field $\mathbf{F}_0$ represents the external load on the shell continuum, and ρ_0 the density of the reference configuration. In this special shell kinematics the variation of the deformation mapping is given by $\delta\Phi = \delta\phi \circ (\phi_0)^{-1}$ with corresponding functions

$$\delta\phi := \delta\varphi + \zeta\delta\mathbf{d}\,, \qquad \delta\varphi : \omega \to \mathbb{R}^3\,, \qquad \delta\mathbf{d} : \omega \to \mathrm{T}_{\mathbf{d}}\mathsf{S}^2\,, \tag{9}$$

where $\mathrm{T}_{\mathbf{d}}\mathsf{S}^2 := \{\delta\mathbf{d} \in \mathbb{R}^3 | \delta\mathbf{d} \cdot \mathbf{d} = 0\}$ is the tangential plane of S^2 in $\mathbf{d}$. In the following the function describing the shell configurations and its variation are summerized as $\boldsymbol{q} = (\varphi, \mathbf{d})^T$, $\boldsymbol{q}_0 = (\varphi_0, \mathbf{d}_0)^T$ and $\delta\boldsymbol{q} = (\delta\varphi, \delta\mathbf{d})^T$.

With the transformation theorem and the surface measure $\mathrm{d}\bar{\boldsymbol{\chi}} = \det(a_{\alpha\beta})\mathrm{d}\boldsymbol{\chi}$ the part of the internal work from (8) splits into two summands:

$$\int_\Omega S^{ij}\delta E_{ij}\mathrm{d}\zeta\mathrm{d}\bar{\boldsymbol{\chi}} = \int_\Omega E_{\alpha\beta}H^{\alpha\beta\iota\pi}\delta E_{\iota\pi}\mathrm{d}\zeta\mathrm{d}\bar{\boldsymbol{\chi}} + \int_\Omega E_{\alpha 3}H_s^{\alpha 3\iota 3}\delta E_{\iota 3}\mathrm{d}\zeta\mathrm{d}\bar{\boldsymbol{\chi}}. \tag{10}$$

- 10.1515/meceng-2016-0016
Downloaded from De Gruyter Online at 09/23/2016 07:41:16AM
via free access

Therefore membrane stretching and bending have no influences on transverse shearing and vice versa. The first term of (10) is further split into

$$\int_\Omega E_{\alpha\beta} H^{\alpha\beta\iota\pi} \delta E_{\iota\pi} \mathrm{d}\zeta \mathrm{d}\bar{\chi} = \int_\omega \frac{1}{2}(a_{\alpha\beta} - A_{\alpha\beta})(H_m^{\alpha\beta\iota\pi} \delta a_{\iota\pi} + H_c^{\alpha\beta\iota\pi} \delta\kappa_{\iota\pi}) \mathrm{d}\bar{\chi} \quad (11)$$

$$+ \int_\omega \frac{1}{2}(\kappa_{\alpha\beta} - \mathcal{K}_{\alpha\beta})(H_c^{\alpha\beta\iota\pi} \delta a_{\iota\pi} + H_b^{\alpha\beta\iota\pi} \delta\kappa_{\iota\pi}) \mathrm{d}\bar{\chi}. \quad (12)$$

With the approximation $G^{ij} = A^{ij}$ the variable ζ can by eliminated by integration, which yields

$$H_m^{\alpha\beta\iota\pi} := \int_{-\frac{h}{2}}^{\frac{h}{2}} H^{\alpha\beta\iota\pi} \mathrm{d}\zeta \ , \quad H_c^{\alpha\beta\iota\pi} := \int_{-\frac{h}{2}}^{\frac{h}{2}} \zeta H^{\alpha\beta\iota\pi} \mathrm{d}\zeta \ , \quad H_b^{\alpha\beta\iota\pi} := \int_{-\frac{h}{2}}^{\frac{h}{2}} \zeta^2 H^{\alpha\beta\iota\pi} \mathrm{d}\zeta. \quad (13)$$

In the same way the integration of the second summand of (10) is executed. The two remaining parts of (8) are integrated over ζ in a similar way, see [15] for more details.

After the thickness variable is eliminated, we discretize the problem spatially, using the same quadrilateral FE approach as in [1]. Therein the midsurface as well as the director field are interpolated locally by bilinear Lagrangian shape functions

$$\boldsymbol{q}^h = \sum_I^{\mathrm{N}} \mathbf{q}_I N^I \ , \qquad \mathbf{q}_I = (\varphi_I, \mathbf{d}_I)^T \in \mathbb{R}^6. \quad (14)$$

The discrete values $\mathbf{q}_I$ are positioned in the nodes of the FE-mesh. The same is done for the reference configuration $\boldsymbol{q}_0$ and the variation $\delta\boldsymbol{q}$. Substituting these approximations into the integrated equation (8), we end up with a DAE for the motion of the discrete nodal variables $\mathbf{q} = (\mathbf{q}_1, \ldots, \mathbf{q}_{\mathrm{N}})$ of the shell model

$$\mathsf{M}\ddot{\mathbf{q}} = -\mathbf{R}(\mathbf{q}) + \mathsf{G}^T(\mathbf{q})\boldsymbol{\lambda} + \mathbf{F} \ , \quad (15)$$

$$0 = \mathbf{g}(\mathbf{q}). \quad (16)$$

The constraint equation (16) and the corresponding force $\mathsf{G}(\mathbf{q})\boldsymbol{\lambda}$ arise from the unit length condition of the director $\|\mathbf{d}\| = 1$, which is enforced in the nodes of the FE-mesh. The equations (15) - (16) are integrated in time making use of the BDF-formula [3].

3. Material model

In [15] a three dimensional orthotropic material model was transferred to the shell formulation. This is possible, if one principal direction of the

- 10.1515/meceng-2016-0016
Downloaded from De Gruyter Online at 09/23/2016 07:41:16AM
via free access

material points into the normal direction of the midsurface in the reference configuration. The variation of the material in the thickness direction due to the skew basis is neglected by the approximation $G^{ij} \approx A^{ij}$. Therefore the components of the material tensor H^{ijkl} do not depend on ζ any more and the integration is straight forward.

In this work we want to include a multi layered material construction in thickness direction. We assume that the layers are firmly connected. Let N be the number of layers in thickness direction. By h_I the height of the I-th layer is given. The thickness h of the whole shell continuum is given by the sum over all layers as: $h = \sum_{I=1}^{\mathrm{N}} h_I$. The material of each layer is assumed to be isotropic or orthotropic, like in [15]. Therefore each layer has its own material tensor C_I^{ijkl} and could be transferred to a shell material H_I^{ijkl} as shown in (7). The coefficients of the material tensor of the whole shell continuum are reproduced by a piecewise defined function

$$H^{ijkl}_{\mathrm{Lam}}(\zeta) = \begin{cases} H^{ijkl}_{1} & \left(\zeta + \frac{h}{2}\right) \in [0, h_1] \\ \vdots & \vdots \\ H^{ijkl}_{\mathrm{N}} & \left(\zeta + \frac{h}{2}\right) \in [h - h_{\mathrm{N}}, h] \end{cases} . \tag{17}$$

In each layer of the shell we make the approximation $G_I^{ij} \approx A^{ij}$, where G_I^{ij} is the metric of I-th layer and A^{ij} those of the midsurface of the whole continuum. Therefore we can examine the integration from (13) over the thickness on each layer and sum up the results

$$H_{\mathrm{m}}^{\alpha\beta\iota\pi} := \int_{-\frac{h}{2}}^{\frac{h}{2}} H^{\alpha\beta\iota\pi}_{\mathrm{Lam}}(\zeta)\mathrm{d}\zeta = \sum_{I=1}^{\mathrm{N}} h_I H_{\mathrm{I}}^{\alpha\beta\iota\pi} , \tag{18}$$

$$H_{\mathrm{c}}^{\alpha\beta\iota\pi} := \int_{-\frac{h}{2}}^{\frac{h}{2}} \zeta H^{\alpha\beta\iota\pi}_{\mathrm{Lam}}(\zeta)\mathrm{d}\zeta = \sum_{I=1}^{\mathrm{N}} \left(\frac{h_I^2}{2} + \left(-\frac{h}{2} + \sum_{J=1}^{I-1} h_J \right) h_I \right) H_I^{\alpha\beta\iota\pi} , \tag{19}$$

$$H_{\mathrm{b}}^{\alpha\beta\iota\pi} := \int_{-\frac{h}{2}}^{\frac{h}{2}} \zeta^2 H^{\alpha\beta\iota\pi}_{\mathrm{Lam}}(\zeta)\mathrm{d}\zeta = \sum_{I=1}^{\mathrm{N}} \left(\frac{h_I^3}{3} + h_I^2 \left(\sum_{J=1}^{I-1} h_J - \frac{h}{2} \right) + h_I \left(\sum_{J=1}^{I-1} h_J - \frac{h}{2} \right)^2 \right) H_I^{\alpha\beta\iota\pi} . \tag{20}$$

These coefficients could be put into (12) without changing anything in the following discretization. If orthotropic materials should be used, two edges of each FE must by parallel to get a constant orientation inside the element, see [15]. Then for each element and each of its layers the orientation of the material is given by one constant angle. As the coefficients from (18)-(20) depend on the reference configuration only, they can be computed in preprocessing.

- 10.1515/meceng-2016-0016
Downloaded from De Gruyter Online at 09/23/2016 07:41:16AM
via free access

In the tire each layer is made of reinforced material, which consists of two isotropic materials: the matrix material (E_m, ν_m) and the material of the fiber (E_f, ν_f). The percentage amount of reinforcements is given by V_f, for the ratio of the matrix material directly follows $V_m = 1 - V_f$. With the help of the so called rules of mixture [9] the orthotropic material data of each layer could be calculated. In this work we us the approach of Halpin and Tsai [8].

4. Unilateral frictional contact

We want to simulate the frictional contact interaction between a rigid road and the shell representing the tire. The contact surface of the road is usually given by a hight profile $\mathfrak{h} : \mathbb{R}^2 \to \mathbb{R}$ as a two dimensional surface

$$\mathbf{X}(s_1, s_2) = \begin{pmatrix} s_1 & s_2 & \mathfrak{h}(s_1, s_2) \end{pmatrix}^T . \tag{21}$$

Its tangential vectors are given by $\mathbf{T}_\alpha := \frac{\partial \mathbf{X}}{\partial s_\alpha}$, which define the normal vector of the surface $\mathbf{N} := \frac{\mathbf{T}_1 \times \mathbf{T}_2}{\|\mathbf{T}_1 \times \mathbf{T}_2\|}$ The contact surface $\mathcal{B}_c$ of the shell is given by a function

$$\mathbf{x}(\chi) = \mathbf{x}(\boldsymbol{q}(\chi), \chi) , \qquad \mathbf{x} : \omega \to \mathbb{R}^3 , \qquad \partial\mathcal{B}_c := \mathbf{x}(\omega) , \tag{22}$$

which depends on the configuration of the deformed shell. We are using the concept of *master*- and *slave*-surface, see [20]. Hence, for every point in the tire surface (*slave*) we are looking for a contact point in the road surface (*master*). The closest distance point $\widetilde{\mathbf{X}}$ of the road surface is defined for a fixed $\mathbf{x} \in \mathcal{B}_c$ as

$$\|\widetilde{\mathbf{X}} - \mathbf{x}\| \leq \|\mathbf{X}(s_1, s_2) - \mathbf{x}\| , \qquad \forall s_1, s_2. \tag{23}$$

For each point of $\mathcal{B}_c$ the distance function is defined as

$$d_{\mathrm{N}}(\mathbf{x}) := (\mathbf{x} - \widetilde{\mathbf{X}})^T \widetilde{\mathbf{N}}, \tag{24}$$

where $\widetilde{\mathbf{N}}$ is the normal vector of the surface in the closest distance point. With this function we can derive the KKT-conditions [20] for the frictionless contact

$$p_{\mathbf{N}} \geq 0 , \qquad d_{\mathbf{N}} \geq 0 , \qquad p_{\mathbf{N}} d_{\mathbf{N}} = 0, \tag{25}$$

where $p_{\mathbf{N}}$ is the normal contact pressure. To ensure (25), we introduce the normal gap function and its variation as

$$g_{\mathbf{N}}(\mathbf{x}) = \begin{cases} 0 & d_{\mathrm{N}}(\mathbf{x}) \geq 0 \\ d_{\mathrm{N}}(\mathbf{x}) & d_{\mathrm{N}}(\mathbf{x}) < 0 \end{cases} , \qquad \delta g_{\mathbf{N}} = \begin{cases} 0 & d_{\mathrm{N}}(\mathbf{x}) \geq 0 \\ \delta \mathbf{x}^T \mathbf{N} & d_{\mathrm{N}}(\mathbf{x}) < 0 \end{cases} . \tag{26}$$

- 10.1515/meceng-2016-0016
Downloaded from De Gruyter Online at 09/23/2016 07:41:16AM
via free access

The normal contact force is given by $p_{\mathbf{N}} = \epsilon_{\mathbf{N}} g_{\mathbf{N}}(\mathbf{x})$ with a constant penalty parameter $\epsilon_{\mathbf{N}} > 0$. Hence, the contribution of the normal contact to the balance of momentum is given by

$$\mathcal{G}_{\mathbf{N}} = \int_{\mathcal{B}_c} \epsilon_{\mathbf{N}} g_{\mathbf{N}} \delta g_{\mathbf{N}} \mathrm{d}\mathbf{x} = \int_{\omega} \epsilon_{\mathbf{N}} g_{\mathbf{N}} \delta g_{\mathbf{N}} \bar{x} \mathrm{d}\chi \ , \tag{27}$$

where $\bar{x}$ is the Jacobian determinant of (22).

4.1. Tangential contact

To compute the frictional contact between the tire and the road, we have to evaluate the path $\mathbf{g_T}$ of a particle in contact on the *master*-surface. Hereby two cases are distinguished: Either the particle is sticking on the surface, hence, there is no relative movement between both surfaces in this point $\dot{\mathbf{g}}_{\mathbf{T}} = 0$, or the particle is sliding on the surface, hence, a reaction force proportional to the normal contact force is acting on the particle $\mathbf{t_T} = \mu p_{\mathbf{N}} \frac{\dot{\mathbf{g}}_{\mathbf{T}}}{\|\dot{\mathbf{g}}_{\mathbf{T}}\|}$, where μ is the coefficient of friction.

To handle both cases, a method from theory of plasticity is used [19]. The glide path is divided in a reversible elastic $\mathbf{g}^e_{\mathbf{T}}$ and a irreversible plastic part $\mathbf{g}^p_{\mathbf{T}}$, such that $\mathbf{g_T} = \mathbf{g}^p_{\mathbf{T}} + \mathbf{g}^e_{\mathbf{T}}$ holds. The elastic part represents sticking. With a penalty stiffness $\epsilon_{\mathbf{T}} > 0$ the corresponding traction force is given by

$$\mathbf{t_T} = \epsilon_T \mathbf{g}^e_{\mathbf{T}} \ . \tag{28}$$

The plastic part of the glide path is given due to an evolution equation. This equation is derived by maximizing the dissipative power of sliding with respect to the traction force $\mathbf{t_T}$, which is additionally restricted by the condition

$$f_C(\mathbf{t_T}) := \|\mathbf{t_t}\| - \mu p_{\mathbf{N}} \leq 0 \ . \tag{29}$$

The solution of this optimization task is given by the following problem: Find $\mathbf{t_T}$ and λ_f such that the equations

$$\dot{\mathbf{g}}^p_{\mathbf{T}} = -\lambda_f \frac{\partial f_c}{\partial \mathbf{t_T}} \ , \tag{30}$$

$$\lambda_f \leq 0 \ , \qquad 0 \geq f_C(\mathbf{t_T}) \ , \qquad \lambda_f f_C(\mathbf{t_T}) = 0, \tag{31}$$

hold, where (31) are the KKT-conditions of the tangential contact. The discrete evolution of the plastic part of the glide path and the discrete traction forces are evaluated by means of the radial return algorithm [7].

- 10.1515/meceng-2016-0016
Downloaded from De Gruyter Online at 09/23/2016 07:41:16AM
via free access

The implicit Euler method is used to evaluate the evolution equation (30). Let $\mathbf{g}_{\mathbf{T}}^{p^n}$ be the plastic part of the tangential gap at time step t^n, then we get for the next time step

$$\mathbf{g}_{\mathbf{T}}^{p^{n+1}} = \mathbf{g}_{\mathbf{T}}^{p^n} + \frac{-\lambda^{n+1}}{\|\mathbf{t}_{\mathbf{T}}^{n+1}\|}\mathbf{t}_{\mathbf{T}}^{n+1}. \tag{32}$$

The two unknowns λ^{n+1} and $\mathbf{t}_{\mathbf{T}}^{n+1}$ are computed such that the KKT-conditions (31) are ensured at t^{n+1}. Therefore a trial stress is computed by assuming that the particle is purely sticking

$$\tilde{\mathbf{t}}_{\mathbf{T}} = \epsilon_T \left(\mathbf{g}_{\mathbf{T}}^{k+1} - \mathbf{g}_{\mathbf{T}}^{p^k}\right). \tag{33}$$

If $0 \geq \tilde{f}_C(\tilde{\mathbf{t}}_{\mathbf{T}})$ holds, the trail stress is accepted $\mathbf{t}_{\mathbf{T}}^{k+1} = \tilde{\mathbf{t}}_{\mathbf{T}}$ and from (31) follows that $\lambda^{n+1} = 0$. Otherwise, if we have $0 < \tilde{f}_C(\tilde{\mathbf{t}}_{\mathbf{T}})$, the trail stress is projected to

$$\mathbf{t}_{\mathbf{T}}^{n+1} = \tilde{\mathbf{t}}_{\mathbf{T}} - \lambda^{n+1}\epsilon_{\mathbf{T}}\frac{\tilde{\mathbf{t}}_{\mathbf{T}}}{\|\tilde{\mathbf{t}}_{\mathbf{T}}\|}. \tag{34}$$

Because $f_c(\mathbf{t}_{\mathbf{T}}^{n+1}) = 0$ must hold in this case, the remaining unknown is given by

$$\lambda_f^{n+1} = \frac{1}{\epsilon_{\mathbf{T}}}(\|\tilde{\mathbf{t}}_{\mathbf{T}}\| - \mu p_{\mathbf{N}}). \tag{35}$$

Now the plastic part of the tangential gap can be computed as in (32).

The variation of the slip path $\mathbf{g}_T$ can be obtained by differentiating the optimality condition of the nearest contact point (23) with respect to time, see [18]. Since the road surface is not in motion and we assume that the normal penetration into the road surface is negligibly small, this variation is given by

$$\delta\mathbf{g}_{\mathbf{T}} = (\mathsf{Id} - \widetilde{\mathbf{N}} \otimes \widetilde{\mathbf{N}})\delta\mathbf{x}. \tag{36}$$

Hence, for the contribution of the tangential contact to the balance of momentum we get

$$\mathcal{G}_{\mathbf{T}} = \int_{\mathcal{B}_c} \mathbf{t}_{\mathbf{t}}\delta\mathbf{g}_{\mathbf{t}}^T \mathrm{d}\mathbf{x} = \int_{\omega} \mathbf{t}_{\mathbf{t}}\delta\mathbf{g}_{\mathbf{t}}^T \bar{x}\mathrm{d}\chi. \tag{37}$$

4.2. Discretization of the contact surface

To incorporate the contact force in the discrete equation of motion (15)-(16), the integrals (27) and (37) must be discretized. This could be done with

- 10.1515/meceng-2016-0016
Downloaded from De Gruyter Online at 09/23/2016 07:41:16AM
via free access

a node to segment approach for example, where the contact is evaluated in the nodes of the FE mesh. As discussed in [15], this approach is not able to detect small obstacles. Therefore, the discretization of the FE formulation with bilinear interpolation inside the element was used, and the contact was evaluated at the Gaussian integration points. In this approach the circumferential discretization degenerates to a polygon with a discrete number of edges. This results in a drawback if the tire is rolling on flat ground: In Fig. 1 the problem is visualized by the comparison of a rolling rigid polygon and a rigid circle.

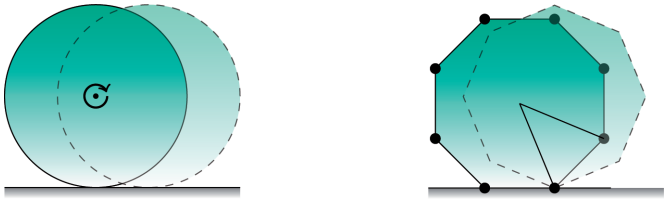

Fig. 1. A rigid ring and a rigid octagon rolling over a flat surface

To eliminate this problem, we use the discrete director in addition to the midsurface points to create the element wise contact shape. This should be done such that the tangential vectors of the surface are perpendicular to the discrete directors in the nodes of the FE mesh. In [11] such an interpolation is realized with a biquadratic shape function. This approach has the drawback that no turning points inside the element could be realized. This may result in strange contact shapes for some situations [12]. To circumvent that problem, we choose the bicubic Hermite-Polynomials as local shape functions for the contact surface. We will explain the procedure on a one dimensional example, where two points $\mathbf{x}_\alpha$ with normal information $\mathbf{d}_\alpha$ should be interpolated.

The cubic Hermite polynomials are given over the interval $[0, 1]$ by

$$\begin{aligned} H_1(s) &= (1+2s)(1-s)^2, & H_2(s) &= s^2(3-2s), \\ H_3(s) &= s(1-s)^2, & H_4(s) &= s^2(s-1). \end{aligned} \tag{38}$$

Therefore the interpolation of the curve reads

$$\mathbf{x}(s) = \mathbf{x}_1 H_1(s) + \mathbf{x}_2 H_2(s) + \mathbf{m}_1 H_3(s) + \mathbf{m}_2 H_4(s). \tag{39}$$

At the end nodes of the interpolation curve we obtain by straightforward computation

$$\mathbf{x}(0) = \mathbf{x}_1\,, \qquad \mathbf{x}(1) = \mathbf{x}_2\,, \qquad \mathbf{x}'(0) = \mathbf{m}_1\,, \qquad \mathbf{x}'(1) = \mathbf{m}_2. \tag{40}$$

- 10.1515/meceng-2016-0016
Downloaded from De Gruyter Online at 09/23/2016 07:41:16AM
via free access

Therefore $\mathbf{m}_\alpha$ must be chosen such that $\mathbf{m}_\alpha \cdot \mathbf{d}_\alpha = 0$ holds. With the help of the rotation matrix

$$\mathsf{R}(\mathbf{d}_\alpha, \mathbf{b}) := \frac{\|\mathbf{b}\|}{\|\mathbf{d}_\alpha \times \mathbf{b}\|} (\mathsf{Id} - \mathbf{d}_\alpha \otimes \mathbf{d}_\alpha) \in \mathbb{R}^{3\times 3} \qquad \text{with} \qquad \mathbf{b} = \mathbf{x}_2 - \mathbf{x}_1, \quad (41)$$

the tangential vectors are given by

$$\mathbf{m}_\alpha = \mathsf{R}(\mathbf{d}_\alpha, \mathbf{b})\mathbf{b}, \quad (42)$$

and $\mathbf{m}_\alpha \cdot \mathbf{d}_\alpha = 0$ holds obviously. Additionally the length of the tangential vectors are equal to the distance between the interpolated points $\|\mathbf{m}_\alpha\| = \|\mathbf{b}\|$. If this approach is used locally to construct a curve from many given points and normals, the direction of tangential vectors of resulting local curves are equal in the nodes, Nevertheless, its magnitudes could differ. Therefore, the curve is not continuously differentiable.

This approach can be easily transferred to a two dimensional surface according to the concept of a tensor product surface, where each edge is interpolated according to the one dimensional approach. To do that a bicubic shape function is used

$$\mathbf{x}(s,t) = \sum_{I=1}^{4} \sum_{j=1}^{4} \mathbf{C}_{IJ} H_I(s) H_J(t). \quad (43)$$

Additionally the mixed derivatives in the nodes of the surface could be defined. We set them to zero $C_{34} = C_{43} = C_{33} = C_{44} = 0$, which correspondence to the so called Ferguson patch [5]. In Fig. 2 the interpolation of such a surface is visualized with the corresponding coefficients from (43).

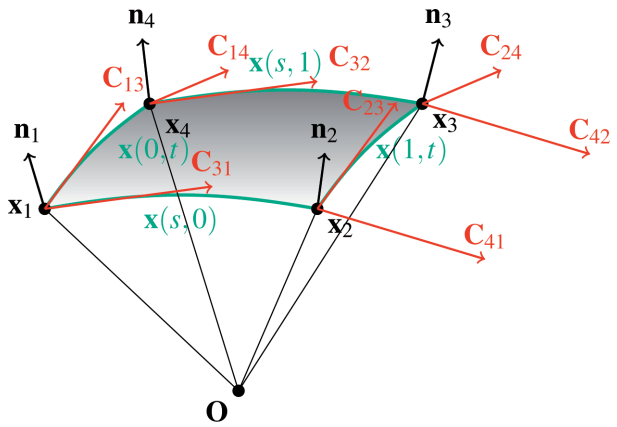

Fig. 2. Tensor product with cubic Hermite-splines as boundary curves

- 10.1515/meceng-2016-0016
Downloaded from De Gruyter Online at 09/23/2016 07:41:16AM
via free access

With this approach the integrals (27) and (37) are element-wise discretized. For the interpolation of the variation $\delta\mathbf{x}$ no tangential or normal information is used. The contact algorithm is evaluated at the discrete Gaussian integration points as in [15].

4.3. Comparison to brush contact

In commercial tire models like [6], the contact between tire and road is modeled by a so called brush models, which is a similar approach to the one presented in this work. In this brush models the penalty stiffnesses are interpreted as the stiffness of the rubber tread blocks and they are used to fit the simulation results to the measurements. Therefore the contact evaluation is mixed up with the material properties of the tire in a very coarse way. In this work the penalty stiffnesses are interpreted purely as auxiliary variables to ensure $d_n \geq 0$ for normal contact and $\mathbf{g_T} = 0$ in case of sticking. Therefore, comparably high values are used for this constants $\epsilon_\mathbf{N} = 10^8$ and $\epsilon_\mathbf{T} = 3 \cdot 10^7$ Especially only a scalar penalty parameter is used in the tangential case, which could be interpreted as an isotropic tangential stiffness.

One way to include the stiffenss of the rubber blocks in the model would be to use the outer surface of the shell continuum $\varphi + h\mathbf{d}$ as contact surface. Therefore, the shearing stiffness of the shell could be used as tangential stiffness of the tread. However, this has not been included in the model presented in this work. One could even think of using a reduced model of the 3D rubber blocks, as additional element between the shell and the contact evaluation. However, these are only ideas and not included in the present work, but eventually will be tackled in further work.

5. Tire simulation

Finally we want to show some classical tire test rig simulations with our model constructed from geometrically exact shells. As comparison we choose the discrete finite-difference based multi layer shell model CDTire/3D [6]. This model has been parametrized such that the experimental results of a real tire on a test trig could be reproduced. Therefore, we may use CDTire/3D to perform numerical experiments for benchmarking. The physical tire has the standardized size *245/40 R 18*. As inner pressure of the tire in all simulation 2.7 [bar] is chosen. As friction coefficient $\mu = 1$ is assumed.

First we want to calibrate the material data of the tire model presented in this work. To do that, we choose a simple vertical stiffness simulation of a tire. Therein the tire is flattened out against a flat rigid surface by deflecting the rim in vertical direction. This implies a vertical reaction force on the rim.

- 10.1515/meceng-2016-0016
Downloaded from De Gruyter Online at 09/23/2016 07:41:16AM
via free access

The relation between deflection and force produce a characteristic curve of the tire.

The net of discrete nodes of the midsurface are given by cylindrical revolution of the tire cross section. The directors are chosen heuristically such that they approximate the normals of the geometrically simple reference surface. The corresponding number of elements in the cross section are 16 and 50 in circumferential direction. A tire is build from different layers of cord reinforced sheets, each of which can be considered a functional layer. Following the natural concept of parameterizing these individual functional layers [6], we are now using the multi layered material model described in Section 3. The tread is segmented in six layers. The matrix material of every reinforced layer is rubber. Starting from inside, the first layer purely consists of rubber, which is modeled as an isotropic material. The second layer is called carcass, its reinforcements are made of synthetic fibers. They are oriented perpendicular to the direction of rotation. In the third and fourth layer steel-cords are used to strengthen the material. The steel wires are oriented mirror-symmetric in both layers concerning the direction of rotation. The fifth layer is called cap ply. It is reinforced with nylon cords, which are directed along the direction of rotation. A layer consisting purely of rubber is the last of the six layers. For the first and the last layer, we choose a isoptropic material model. For the others an orthotropic material model is chosen, whose material coefficients are computed by the approach of Halpin and Tsai [8], using the material data from Table 1 with the angle α measured with respect to the direction of rotation. For the sidewall the two steel-cord layers and the cap-ply are substituted by layers with the same thickness consisting of isotropic rubber.

Table 1.

Optimized material properties of the different layers of the tire

	E_m [N/m^2]	ν_m	E_f [N/m^2]	ν_f	V_f	α [deg]	h_i [m]
Rubber	$7,39 \cdot 10^6$	0,5					$1.55 \cdot 10^{-3}$
Carcass	$7,39 \cdot 10^6$	0,5	$1,33 \cdot 10^8$	0	0,26	90	$1,04 \cdot 10^{-3}$
Steel-cord	$7,39 \cdot 10^6$	0,5	$1,98 \cdot 10^{11}$	0	0,17	−24	$0,9 \cdot 10^{-3}$
Steel-cord	$7,39 \cdot 10^6$	0,5	$1,98 \cdot 10^{11}$	0	0,17	24	$0,9 \cdot 10^{-3}$
Cap-ply	$7,39 \cdot 10^6$	0,5	$3,43 \cdot 10^9$	0	0,26	0	$0,65 \cdot 10^{-3}$
Rubber	$7,39 \cdot 10^6$	0,5					$2.5 \cdot 10^{-3}$

The material informations of Table 1 are adopted from a datasheet of a tire. The elastic modulus of the rubber matrix and the synthetic fibers in the carcass are optimized such that the result of vertical stiffness simulation

- 10.1515/meceng-2016-0016
Downloaded from De Gruyter Online at 09/23/2016 07:41:16AM
via free access

coincides with the reference solution, see Fig. 3. The optimization was performed fully automatized, by minimizing the squared distance between the two curves.

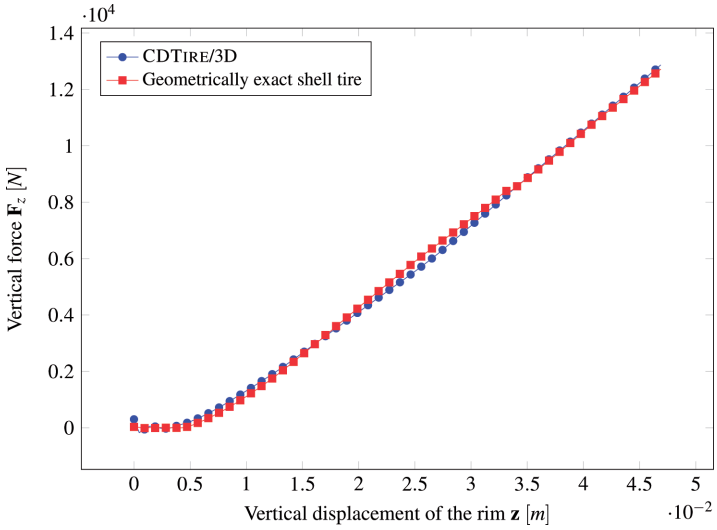

Fig. 3. Reaction force on the rim, due to the flattening of the tire against a flat rigid road

5.1. Lateral and longitudinal stiffness

We want to have a look at the lateral and the longitudinal stiffness of the tire in the following simulation. Therefore, the tire is deflected against a flat rigid surface until a vertical reaction force of 4 [kN] is reached. In the lateral stiffness simulation the rim is deflected perpendicular to the running direction of the tire. This implies a lateral reaction force on the rim. In the longitudinal stiffness simulation the rim is deflected in the running direction of the tire, while all rotations are locked. Therefore, a longitudinal reaction force is acting on the rim. Again the results of the simulation are compared with those of CDTire/3D.

In Fig. 4 the simulation results of the lateral stiffness simulation are visualized.

The lateral deflection of the rim is plotted against the reacting force. After the lateral force reaches the size of the vertical force the tire is sliding with a constant reaction force in lateral direction over the flat ground. Because the simulation results of the tire model developed in this work match with those of CDTire/3D, the lateral stiffness of the tire is predicted correctly with our model without doing any additional parameter modification.

- 10.1515/meceng-2016-0016
Downloaded from De Gruyter Online at 09/23/2016 07:41:16AM
via free access

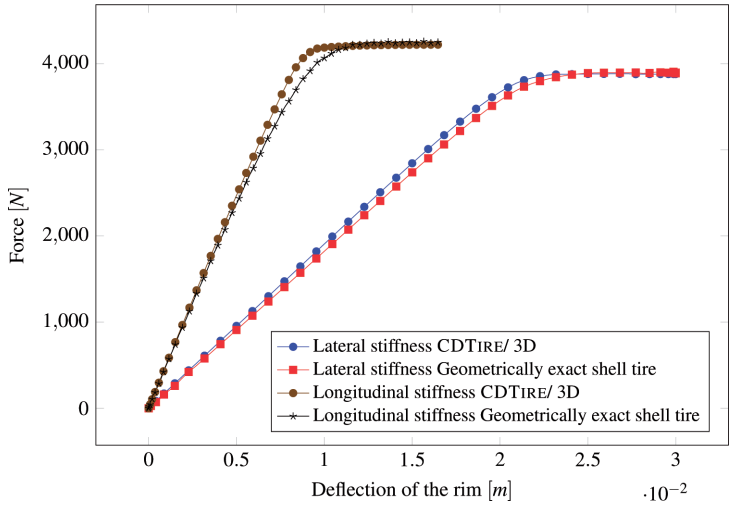

Fig. 4. Lateral and longitudinal stiffness of the tire loaded with 4 [kN] in vertical direction

The results of the longitudinal stiffness simulation can be seen in Fig. 4. Therein, the longitudinal deflection of the rim is plotted against the reaction force. The tire again starts to slide on the surface with a constant reaction force, if the longitudinal reaches the vertical force. At the beginning of the simulation, the whole contact patch is sticking on to the road surface. In this situation both curves match pretty well. This indicates that the structural stiffness of the tire is predicted in a correct way. When the contact points start to slide, both curves do not match perfectly together. This could be because the forces in the contact patch are not predicted accurate enough. However, this results are again achieved without any further adjustments on the parameters.

5.2. Lateral slip

In this section, we want to show a first dynamical simulation. The rim is moved with a constant velocity of 10 [m/s] in running direction of the tire over a flat surface with a constant vertical deflection, such that a reaction force of 4 [kN] is acting on the rim. The rotation of the rim due to its longitudinal movement and contact is realized via a co-simulation of the tire model and the rim, see [15]. The duration of this simulation is five seconds. In this time the rim is rotated about its vertical axis to simulate cornering[2].

[2] The vehicle drives through a curve.

- 10.1515/meceng-2016-0016
Downloaded from De Gruyter Online at 09/23/2016 07:41:16AM
via free access

The time signal of the corresponding angle is given by

$$\alpha(t) = \begin{cases} \frac{15\pi}{180} \sin\left(\frac{2(t-0.5)}{\pi}\right) & 0.5 \leq t \leq 4.5 \\ 0 & \text{otherwise} \end{cases} . \tag{44}$$

In the literature, this angle is called slip angle. Due to cornering the tire produces a lateral force on the rim. In Fig. 5 the simulation results are visualized.

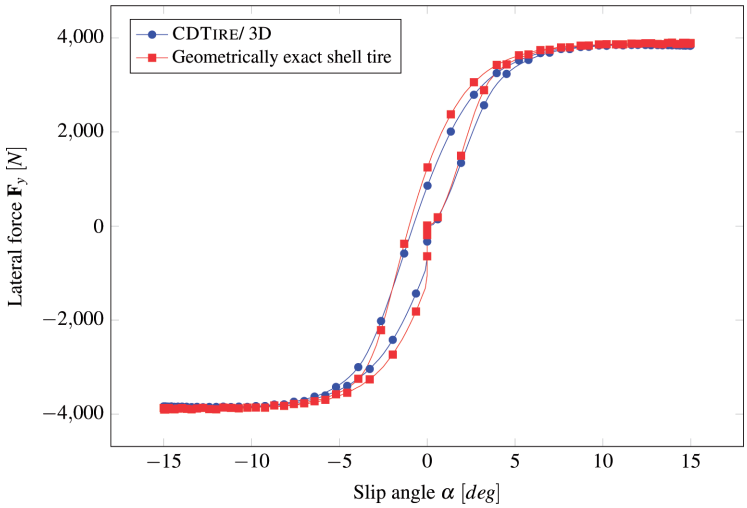

Fig. 5. Lateral slip at $v = 10$ [m/s]

Therein, the lateral force is plotted against the slip angle α, which results in a curve that is characteristic for a tire. The simulation result of the tire model developed in this work matches favorably to the reference solution. So, we predicted the cornering behavior of the tire quite well without doing any adjustment of the model parameters. In Fig. 5 a hysteresis could be seen because of the movement of material point through the contact patch.

5.3. Longitudinal slip

Finally we want to simulate the accelerating and breaking of a tire. To do that, a longitudinal slip experiment is realized. Therein, the rim is moving with a constant velocity in rotational direction, while the rotation velocity of the rim is varied in time. To examine the simulation the rotation velocity ω_0 of free rolling[3] tire must be evaluated. The longitudinal slip κ is defined

[3] Free rolling is defined such that no torque is acting on the rim about the rotation axis of the tire.

- 10.1515/meceng-2016-0016
Downloaded from De Gruyter Online at 09/23/2016 07:41:16AM
via free access

as relative difference of the current rotational velocity ω and free rolling velocity ω_0

$$\kappa := \frac{\omega - \omega_0}{\omega_0} \,. \tag{45}$$

The simulation is executed in the time interval $[0, 5]$. In contrast to the lateral slip simulation in this experiment also the rotation of the rim is prescribed. This is done via a time signal for the longitudinal slip, which implies the rotational velocity

$$\omega(t) = (1 + \kappa(t))\omega_0 \quad \text{with} \quad \kappa(t) = \begin{cases} \sin\left(\frac{2(t-0.5)}{\pi}\right) & 0.5 \le t \le 4.5 \\ 0 & \text{else} \end{cases} . \tag{46}$$

Because of the different model approaches, both simulated tire models have different rotation velocities ω_0 for the same translation velocity $v = 10$ [m/s]. However, because the longitudinal slip is defined relative to ω_0, we can compare both models.

In Fig. 6 the results of both simulations are visualized. Therein, the longitudinal slip is plotted against the longitudinal force. Both simulation results match quite well. Similar as in the longitudinal stiffness simulation differences occur, when the particles in the contact patch start sliding. Due to the stick and slip history of the material points moving through the contact patch, there is a hysteresis in the graph in Fig. 6 similar as in the lateral slip simulation.

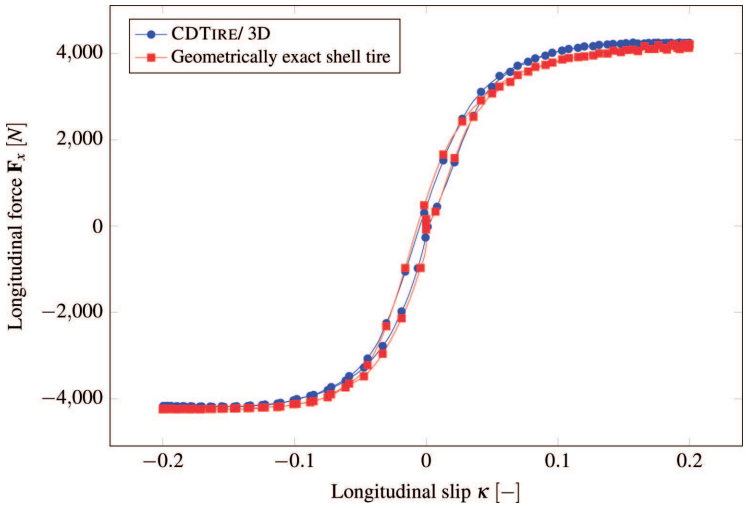

Fig. 6. Longitudinal slip at $v = 10$ [m/s]

- 10.1515/meceng-2016-0016
Downloaded from De Gruyter Online at 09/23/2016 07:41:16AM
via free access

5.4. Discussion of the results

In the simulations it could be shown that the simulation model could predict the tire characteristic curves, after the material has been adjusted only for the vertical stiffness experiment. As reference the commercial tire model CDTire/3D was used, which has been parametrized by real tire measurements. In comparison of the computing time of both models, the model presented in this work is of factor eight slower then CDTire/3D. But in comparison to 3D **FE**-models, which has similar predictive behavior, if the material data is known, the geometric exact shell model is at least a factor 100 faster.

In this work, only purely longitudinal or lateral slip was simulated. A combined slip experiments, which occurs in vehicle dynamics for example when the car is cornering and braking at the same time, was not investigated. In these scenario the pressure distribution in the contact patch becomes important, as in the single slip experiments. It could also be, that in this application case the stiffness of the tread blocks has to be taken into account, see subsection 4.3. To investigate the combined slip experiment will be the topic of further work.

A more detailed discussion of the geometric exact shell tire model and its capabilities could be found in [16].

6. Conclusion and outlook

In this work the tire model from [15] is improved by a multilayer material model and a more complex contact model, which includes lateral contact. With this enhanced model it is possible to predict the dynamical behavior of a tire, while the adjustment of the parameters is done only via a simple vertical stiffness experiment.

Manuscript received by Editorial Board, September 16, 2015;
final version, June 07, 2016.

REFERENCES

[1] Betsch P., Sänger N.: On the use of geometrically exact shells in a conserving framework for flexible multibody dynamics. Computer Methods in Applied Mechanics and Engineering, 198(17), 1609-1630, 2009.
[2] Bonet J.: Nonlinear continuum mechanics for finite element analysis. Cambridge University Press, 1997.
[3] Brenan K.E., Campbell S.L., Petzold L.R.: Numerical solution of initial-value problems in differential-algebraic equations, vol. 14. Siam, 1996.
[4] Chapelle D., Bathe K.-J. et al.: The finite element analysis of shells: fundamentals. Springer, 2011.

- 10.1515/meceng-2016-0016
Downloaded from De Gruyter Online at 09/23/2016 07:41:16AM
via free access

[5] Farin G.E.: Curves and surfaces for computer-aided geometric design: a practical code. Elsevier, 1996.
[6] Gallrein A., Bäcker M., Gizatullin A.: Structural MBD tire models: Closing the gap to structural analysis-history and future of parameter identification. SAE Technical Paper, 2013.
[7] Giannakopoulos A.: The return mapping method for the integration of friction constitutive relations. Computers & structures, 32(1), 157-167, 1989.
[8] Halpin J.C., Kardos J.L.: The Halpin-Tsai equations: A review. Polymer Engineering & Science, 16(5), 344-352, 1976.
[9] Jones R.M.: Mechanics of composite materials. CRC Press, 1998.
[10] Lugner P., Plöchl M.: Tyre model performance test: first experiences and results. Vehicle System Dynamics, 43(1), 48-62, 2005.
[11] Nagata T.: Simple local interpolation of surfaces using normal vectors. Computer Aided Geometric Design, 22(4), 327-347, 2005.
[12] Neto D., Oliveira M., Menezes L., Alves J.: Improving nagata patch interpolation applied for tool surface description in sheet metal forming simulation. Computer-Aided Design, 45(3), 639-656, 2013.
[13] Pacejka H.B., Bakker E.: The magic formula tyre model. Vehicle System Dynamics, 21(S1), 1-18, 1992.
[14] Poldneff M.J., Heinstein M.W.: Computational mechanics of rubber and tires. Modeling and Simulation in Polymers, p. 385-403, 2010.
[15] Roller M., Betsch P., Gallrein A., Linn J.: On the use of geometrically exact shells for dynamic tire simulation. Multibody Dynamics, p. 205-236. Springer, 2014.
[16] Roller M.: Dynamische Reifensimulation mit geometrisch exakten Schalen (Dynamic tire simulation with geometrically exact shells). PhD Thesis, Karlsruhe Institute of Technology, 2016 (in German).
[17] Simo J.C., Fox D.D.: On a stress resultant geometrically exact shell model. Part I: Formulation and optimal parametrization. Computer Methods in Applied Mechanics and Engineering, 72(3), 267-304, 1989.
[18] Wriggers P.: Finite element algorithms for contact problems. Archives of Computational Methods in Engineering, 2(4), 1-49, 1995.
[19] Wriggers P.: Nonlinear finite element methods, vol. 4. Springer, 2008.
[20] Wriggers P., Laursen T.A.: Computational contact mechanics. Springer, 2008.

Udoskonalony model opony do symulacji dynamicznej oparty na powłokach geometrycznie dokładnych

Streszczenie

Praca przedstawia opracowanie modelu opony w oparciu o koncepcję powłoki geometrycznie dokładnej. Dyskretyzację przeprowadzono z pomocą izoparametrycznych czworokątnych elementów skończonych. Do interpolacji wykorzystano wielomiany Lagrange'a, zarówno dla powierzchni pośrednich, jak i pola kierunku. Zastosowano formułę różniczkowania wstecznego jako metodę dyskretyzacji czasowej dla wynikowych równań różniczkowo-algebraicznych. Wprowadzono wielowarstwowy model materiału powłoki geometrycznie dokładnej by opisać anizotropowe właściwości materiału opony. W celu wyznaczenia interakcji między oponą i twardą nawierzchnią drogi wprowadzono sformułowanie jednostronnego kontaktu ciernego. Uzyskano tą drogą specjalny międzypowierzchniowy element kontaktowy, który odtwarza kształt opony.

- 10.1515/meceng-2016-0016
Downloaded from De Gruyter Online at 09/23/2016 07:41:16AM
via free access